

Doping and two distinct phases in strong-coupling kagome superconductors

Haitao Yang^{1,2,3,4#}, Yuhang Zhang^{1,2#}, Zihao Huang^{1,2#}, Zhen Zhao^{1,2#}, Jinan Shi², Guojian Qian^{1,2}, Bin Hu^{1,2}, Zouyouwei Lu^{1,2}, Hua Zhang^{1,2}, Chengmin Shen^{1,2}, Xiao Lin², Ziqiang Wang⁵, Stephen J. Pennycook², Hui Chen^{1,2,3,4*}, Xiaoli Dong^{1,2,4*}, Wu Zhou^{2,3*}, and Hong-Jun Gao^{1,2,3,4*}

¹ *Beijing National Center for Condensed Matter Physics and Institute of Physics, Chinese Academy of Sciences, Beijing 100190, PR China*

² *School of Physical Sciences, University of Chinese Academy of Sciences, Beijing 100190, PR China*

³ *CAS Center for Excellence in Topological Quantum Computation, University of Chinese Academy of Sciences, Beijing 100190, PR China*

⁴ *Songshan Lake Materials Laboratory, Dongguan, Guangdong 523808, PR China*

⁵ *Department of Physics, Boston College, Chestnut Hill, MA, USA*

[#]These authors contributed equally to this work

^{*}Correspondence to: hjgao@iphy.ac.cn; wuzhou@ucas.ac.cn; dong@iphy.ac.cn; hchenn04@iphy.ac.cn

The vanadium-based kagome superconductor CsV_3Sb_5 has attracted tremendous attention due to its unconventional anomalous Hall effect (AHE), its charge density waves (CDWs), and a pseudogap pair density wave coexisting with unconventional strong-coupling superconductivity (SC). The origins of time-reversal symmetry breaking (TRSB), unconventional SC, and their correlation with different orders in this kagome system is of great significance, but, so far, is still under debate. Doping by the chemical substitution of V atoms in the kagome layer provides the most direct way to reveal the intrinsic physics that originates from the kagome lattice, but remains unexplored. Here, we report, for the first time, the synthesis of Ti-doped CsV_3Sb_5 single crystals with controllable carrier doping concentration. The Ti atoms directly substitute for V in the vanadium kagome layers. Remarkably, the Ti-doped CsV_3Sb_5 SC phase diagram shows two distinct SC phases. The lightly-doped SC phase has a V-shaped gap pairing, coexisting with CDWs, indicating a strong-coupling unconventional SC nature. The other SC phase has a U-shaped gap pairing without CDWs, displaying a conventional SC feature. This is the first observation of the two distinct phases in superconductors, revealed through Ti doping of CsV_3Sb_5 . These findings pave a new way to synthesise doped CsV_3Sb_5 and represents a new platform for tuning the superconducting pairing and multiple orders in kagome superconductors.

The newly discovered kagome metals AV_3Sb_5 ($A=K, Rb, Cs$) have attracted tremendous research interest as a novel platform to study the interplay between nontrivial band topology, superconductivity (SC), and multiple density waves.¹⁻⁶ The AV_3Sb_5 carries no magnetic order at low temperature but exhibits an unconventional anomalous Hall effect (AHE) that is usually observed in ferromagnetic materials⁶⁻⁸. Most recently, correlated electronic state and roton pair density wave (PDW) have been observed in the strong-coupling kagome superconductor CsV_3Sb_5 ^{9,10}. Time-reversal symmetry breaking (TRSB) was proposed to originate from the unconventional charge density waves (CDW)^{1,11,12}, but this is still under debate¹³⁻²⁵. Therefore, the nature of the superconducting state remains elusive. Theoretically, CsV_3Sb_5 has a Z_2 nontrivial topological band structure with topological surface states, indicating an unconventional superconductor^{4,26}, while some theoretical works propose the conventional s-wave SC in CsV_3Sb_5 . Experimentally, transport evidence for gap nodes²⁷ and gapless core states in magnetic-field induced vortices² have been reported, while tunneling diode oscillator²⁸ and nuclear quadrupole resonance²⁹ experiments showed the nodeless superconductivity nature of CsV_3Sb_5 . Therefore, full understanding of the pairing of the superconducting state and its correlation with the kagome geometry, TRSB and unconventional density waves remains an important issue to be urgently resolved.

Tuning different orders *via* mechanisms like carrier doping or external pressure provides an effective way to study the nature of the superconducting state and its correlation with the other orders³⁰⁻³³. In experiments, selective oxidation of exfoliated thin flakes is reported to have a notable effect on both SC and CDW orders in the Cs variant. A superconducting dome was obtained as a function of doping content³⁴. Furthermore, the pressure effects have recently been studied, showing that superconducting domes arise upon applied pressure with enhanced SC transition temperature and no sign of a structural phase transition^{5,35-40}. Although tuning of T_c has been achieved in these works, the microscopic origin of SC pairing and its correlation with the charge orders are still elusive. As the unusual properties are believed to come from the proximity of the V $3d$ orbitals close to the van Hove singularity (vHs), chemical substitution of the transition metal V in the kagome layer should be an effective way to directly tune the vHs and unveil the origin of intrinsic electronic structures of AV_3Sb_5 , but remains so far unexplored.

In this Letter, we report the synthesis of titanium-doped $CsV_{3-x}Ti_xSb_5$ crystals with controlled carrier doping concentration for the first time. We confirm that the Ti atoms mainly substitute the V sites in the VSb kagome layer through high-resolution scanning transmission electron microscopy (STEM) chemical imaging. Low temperature scanning tunneling microscopy/spectroscopy (STM/S) reveals that the $2a_0 \times$

$2a_0$ and $4a_0$ CDWs evolve from long-range to short-range modulations, and gradually disappear as the titanium content, x , increases. The dI/dV spectra show that the SC transitions from V-shaped pairing at $x=0.03$ to U-shape pairing at $x=0.15$. The magnetic susceptibility and transport measurements indicate that, as x increases, both the onset temperatures of CDW gradually decrease and are absent at around $x=0.15$. In addition, as the doping content increases, T_c drops to a minimum around $x=0.04$, then increases to 3.5 K at around $x=0.15$, showing a double-dome shape in the phase diagram. The two dome regions show very different superconducting transition behavior in the transport measurement. These results demonstrate that the $\text{CsV}_{3-x}\text{Ti}_x\text{Sb}_5$ exhibits two distinct SC phases. The lightly doped region shows an unconventional SC phase with a V-shape gap pairing, coexisting with CDWs, while the other phase displays a conventional SC phase with a fully-gapped pairing.

Synthesis of the Ti-doped $\text{CsV}_{3-x}\text{Ti}_x\text{Sb}_5$ single crystals

We have successfully grown Ti-doped $\text{CsV}_{3-x}\text{Ti}_x\text{Sb}_5$ crystals with different doping ratios ranging from $x=0$ to 0.15. The as-grown Ti-doped $\text{CsV}_{3-x}\text{Ti}_x\text{Sb}_5$ single crystals (Methods) exhibit a stacking sequence of Cs-Sb2-VSb1-Sb2-Cs layers with hexagonal symmetry (space group $P6_3/mmm$). In the VSb1 layer, the kagome sub-lattice of vanadium is interwoven with a simple hexagonal sub-lattice formed by the Sb1 atoms. The similar ionic radii of Ti^{4+} (60.5 pm) and V^{3+} (61.5 pm) ions suggest the possibility of Ti substitution at the V sites in the kagome lattice (Fig. 1a). A typical $\text{CsV}_{3-x}\text{Ti}_x\text{Sb}_5$ crystal with a lateral size of over 1 cm and regular shape is shown in Fig. 1b. The representative x-ray diffraction (XRD) pattern of the $\text{CsV}_{3-x}\text{Ti}_x\text{Sb}_5$ single crystal only shows the (00l) diffraction peaks and confirms the pure phase of the as-grown single crystal, with a preferred [001] orientation (Fig. 1c). The lattice parameters a , b , and c are measured to be 5.521, 5.521 and 9.336 Å, respectively, by single crystal diffraction, which are slightly smaller than those of pristine CsV_3Sb_5 (5.548, 5.548, and 9.349 Å, respectively) due to the smaller ionic radius of Ti^{4+} . The Ti-doped $\text{CsV}_{3-x}\text{Ti}_x\text{Sb}_5$ single crystal is thin and can show some regular hexagonal morphology with a natural tendency to exfoliate (Fig.1 d). The doping contents of $\text{CsV}_{3-x}\text{Ti}_x\text{Sb}_5$ are determined by both EDS and the inductively coupled plasma (ICP), for which the measurement results are well consistent. The doping contents of a typical Ti-doped $\text{CsV}_{3-x}\text{Ti}_x\text{Sb}_5$ single crystal determined by energy-dispersive x-ray spectroscopy (EDS) is $x=0.15$ as shown in Fig. 1e, corresponding to the 5 % substitution ratio of V.

Determination of the Ti substitution position

To confirm the successful doping of Ti into the CsV_3Sb_5 lattice, we carried out atomic-scale structural and chemical analysis on cross-sectional samples using aberration corrected STEM. Figures 2a and b show the simultaneously acquired STEM annular bright-field (ABF) image and high-angle annular dark-field (HAADF) Z-contrast image⁴¹ of the Ti-doped $\text{CsV}_{3-x}\text{Ti}_x\text{Sb}_5$ ($x=0.15$) sample along the [100] projection, with the structural models overlaid. Both images clearly reveal the perfect crystalline structure of the Ti-doped sample without noticeable structural defects, suggesting that Ti doping does not degrade the crystal quality. The distinct sequential layers of Cs-Sb2-VSb1-Sb2-Cs were further confirmed by the elemental mapping shown in Figure S1. Chemical analysis via electron energy-loss spectroscopy (EELS) unambiguously confirms the presence of Ti dopants (Fig. 2c), with the overall Ti substitution of V measured to be $\sim 5\%$, which is consistent with the EDS and ICP measurements. The spatial distribution of the Ti dopants is revealed by the atomic-resolution chemical mapping shown in Figs. 2d-f. By comparing the simultaneously acquired V map (Fig. 2d) and Ti map (Fig. 2e), it is clear that most of the Ti dopants are located in the VSb1 layer, coinciding with the V atomic columns. Imaging and chemical analysis of the cross-sectional sample along the [210] projection (Figure S2) reveal similar information. These results, thus, suggest that the majority of the Ti dopants is substituting the V sites in the CsV_3Sb_5 lattice, with a tiny amount forming interstitial dopants in the Cs and Sb layers.

STM/S investigation of the Ti-doped CsV_3Sb_5 samples

We then studied the evolution of CDW on the surface of the $\text{CsV}_{3-x}\text{Ti}_x\text{Sb}_5$ samples with various Ti doping contents at the atomic scale by low temperature STM/S (Fig. 3a-j). In the STM measurements, almost all the surface regions show large-scale Cs surface topography. Large-scale Sb surface topography was rarely observed. Thus, we applied the STM manipulation method to sweep the top Cs atoms away to expose large-scale Sb surfaces⁹. In both STM topography ($T(\mathbf{r}, V)$) and dI/dV maps ($dI/dV(\mathbf{r}, V)$) of the large-scale Sb surface, we found that, as compared to the undoped CsV_3Sb_5 sample^{2,9,10,35,42-44} many small dark spots appear and randomly distribute in the STM images. Atomically resolved STM images demonstrate that the Sb lattice remains continuous across the dark spots (inset in Fig. 3a), which indicates that the dark spots originate from electron scattering near the Ti dopants in the underlying VSb1 layer. Furthermore, we analyzed the height histogram of the STM images of the Sb surface and found that the area density of the dark spots shows a positive correlation with the dopant contents (Fig. 3k and Fig. S3), which further

demonstrates that the dark spots in the STM images originate from Ti dopants in the underlying VSb1 kagome layer.

In addition to the emergence of dark spots, there are significant changes of the CDW in both STM images and dI/dV mapping of the Ti-doped $\text{CsV}_{3-x}\text{Ti}_x\text{Sb}_5$ samples as compared with the undoped sample. We find that the bi-directional $2a_0 \times 2a_0$ (green circles in Fig. 3c) and unidirectional $4a_0$ CDWs (red squares in Fig. 3c) at all energies (details in Fig. S4) are preserved for the lightly doped $\text{CsV}_{3-x}\text{Ti}_x\text{Sb}_5$ samples ($x=0.03$ and $x=0.04$) (Figs. 3a-f). In addition, the single-domain 1Q- $4a_0$ CDW in the $60 \text{ nm} \times 60 \text{ nm}$ area in the $x=0.03$ sample (Fig. 3a) split into two or three domains (highlighted by the blue and green dotted lines in Fig. 3d) in the $x=0.04$ sample, indicating that the 1Q- $4a_0$ CDW evolves from long-range to short-range order. Eventually, both $2a_0 \times 2a_0$ and $4a_0$ CDWs almost disappear in the Fourier transform of the topography and dI/dV mapping of the $x=0.15$ sample (Figs. 3g-i). Just small patches of local $4a_0$ CDW domains can be observed in the STM images (Fig. 3j).

The simultaneous suppression and disappearance of long-range $2a_0 \times 2a_0$ and $4a_0$ charge orders strongly indicates that these two CDWs are intertwined with each other. It should be noticed that, the bidirectional $4/3a_0$ PDW peaks⁹ (labeled by pink circles in Fig. S4a,b) in the Fourier transform of dI/dV maps at low energy ($< 5 \text{ meV}$) are suppressed at $x=0.03$ and 0.04 sample but invisible at the $x=0.15$ sample (Fig. S4c), which suggests that the PDW is intertwined with $2a_0 \times 2a_0$ and $4a_0$ CDWs. In addition, accompanying the disappearance of $2a_0 \times 2a_0$ and $4a_0$ CDWs in the $x=0.15$ doped sample, the 1D stripe-like quasiparticle interference (QPI) patterns, labelled as \mathbf{q}_2 in previous reports of undoped CsV_3Sb_5 ¹⁰, are also absent, indicating that the intrinsic rotation symmetry breaking has been restored (Fig. S4).

To study the microscopic evolution of superconductivity in the doped $\text{CsV}_{3-x}\text{Ti}_x\text{Sb}_5$ samples, we lowered the sample temperature to 400 mK and collected a series of dI/dV spectra. We find that the $x=0.03$ doped sample shows a V-shaped SC paring (blue curve in Fig. 3l) while the $x=0.15$ doped sample shows a fully gapped U-shaped paring (red curve in Fig. 3l). The V-shaped SC gap in the $x=0.03$ doped sample is slightly smaller than that of the undoped sample (black curve), and the zero-bias conductance is much higher than that in the undoped sample, indicating the decrease of T_c . For the $x=0.15$ doped sample, the SC paring is totally different from the undoped and lightly doped samples, demonstrating the transition into a new SC phase. The new SC phase may emerge from a normal state without CDW due to the change of the carrier concentration and the electronic states.

Susceptibility and transport properties of the Ti-doped CsV_{3-x}Ti_xSb₅

Finally, we investigated the responses of CDW and superconducting transitions to the doping of Ti in CsV_{3-x}Ti_xSb₅ single crystals via the combination of magnetization, specific heat capacity, and electrical transport measurements. The CDW transition temperature shows an obvious decrease from ~94 K to ~60 K with increasing doping contents, as evidenced by kinks in the temperature-dependent resistivity curves of the Ti-doped CsV_{3-x}Ti_xSb₅ ($x=0, 0.03$, and 0.04) crystals (Fig. 4a). Then the kink fades out in the Ti-doped CsV_{3-x}Ti_xSb₅ ($x=0.09$ and 0.15) indicating the absence of CDWs. The temperature-dependent magnetization and specific heat-capacity measurements (Fig. S5a and b) also provide strong evidence for the undetectability of CDWs in the Ti-doped CsV_{3-x}Ti_xSb₅ ($x=0.09$ and 0.15).

To further investigate the doping effect on the normal state properties of this kagome superconductor system, systematic electrical transport measurements were conducted. Firstly, we measured the in-plane angular-dependent magnetoresistance (AMR) of the CsV_{3-x}Ti_xSb₅ ($x=0.15$) crystal under a field of 5 T at different temperatures above T_c . The ratios of $\Delta R/R_{\min} = [R(\theta, T) - R_{\min}(T)]/R_{\min}(T) \times 100\%$ are summarized in Fig. S5c by polar-coordinate plots, showing an isotropic nature, in contrast to that of undoped CsV₃Sb₅^{45,46}. This indicates clearly the absence of the two-fold rotational symmetry, consistent with the absence of the 1Q-4a₀ CDW and anisotropic QPI patterns in the STM/S measurements of $x=0.15$ doped sample. Secondly, we performed field-dependent Hall measurements of CsV_{3-x}Ti_xSb₅ crystals with different doping contents at various temperatures (Fig. S6a,b,c,d).

Moreover, the doping effects on the superconductivity in CsV_{3-x}Ti_xSb₅ single crystals with x between 0 and 0.15 were examined by diamagnetism measurements. Bulk superconductivity with onset temperature T_c^M is evidenced by the magnetic susceptibilities corrected for demagnetization factor under zero-field cooling (ZFC) and field cooling (FC, 1 Oe along the c axis), as shown in Fig. 4b. It clearly shows that T_c^M decreases to about 2.0 K at $x=0.04$ doping and then increase to 3.0 K and 3.5 K at $x=0.09$ and $x=0.15$ doping, respectively. The onset superconducting transition temperature (T_c^R) derived from the temperature-dependent normalized resistivity of the undoped CsV₃Sb₅ occurs above 4.0 K, about 1.0 K higher than that of the CsV_{3-x}Ti_xSb₅ ($x=0.15$) crystal (Fig. S5d). However, after applying different magnetic fields from 0.02 to 1 T, the T_c^R of the undoped CsV₃Sb₅ shifts to lower temperatures with a relatively small ΔT , resembling the features of broad SC transitions observed in copper-oxide and iron-based high temperature superconductors⁴⁷⁻⁴⁹, while the T_c^R of the Ti-doped CsV_{3-x}Ti_xSb₅ ($x=0.15$)

decreases rapidly with applied fields showing a conventional superconductivity behavior similar with that of MgB_2 ⁵⁰.

Shown in Fig. 4c is the phase diagram of $\text{CsV}_{3-x}\text{Ti}_x\text{Sb}_5$ single crystals, where the onset temperatures of CDW and superconductivity, together with their amplitude, are summarized as a function of doping content. T_{CDW} is depressed with increasing Ti doping and become absent around $x=0.09$, accompanied by the strongly correlated evolution of the signal amplitude (Fig. 4c upper panel). In addition, the $\text{CsV}_{3-x}\text{Ti}_x\text{Sb}_5$ system shows two superconducting domes. The T_c decreases from ~ 3.5 K of the undoped sample to ~ 2.0 K of the $x=0.04$ doped sample in the first dome. In this dome (the SC-I phase), the superconducting phase exhibits a V-shape pairing gap (Fig. 3l) and broadening transition behavior under magnetic field (Fig. S5d, dashed lines), indicating a nodal superconducting phase. In the second dome, the T_c increases from ~ 2.0 K ($x=0.04$) to ~ 3.5 K ($x=0.15$). The superconducting phase in the second dome (the SC-II phase) exhibits a U-shape pairing gap (Fig. 3l) and sharp SC transition at the expense of T_c under magnetic field (Fig. S5d, solid lines), indicating a nodeless superconducting phase.

In summary, we have studied the evolution of CDW and SC in Ti-doped $\text{CsV}_{3-x}\text{Ti}_x\text{Sb}_5$ samples where the Ti atoms directly substitute the V sites in the VSb1 kagome layer. $2a_0 \times 2a_0$ and $4a_0$ CDWs are both suppressed with the increasing doping content of Ti. Furthermore, the phase diagram shows two distinct SC domes where the first dome is characteristic of a V-shape nodal pairing while the second dome features a U-shape nodeless pairing. To our knowledge, the Ti-doped $\text{CsV}_{3-x}\text{Ti}_x\text{Sb}_5$ is the first superconductor reported so far that two distinct SC phases emerge upon chemical doping at ambient pressure, correlating with CDW. Based on this pathway, with other dopants into the AV_3Sb_5 ($A=\text{K}, \text{Rb}, \text{Cs}$) kagome superconductors, it is expected that new kinds of superconductors with novel physical properties can be created. The present work provides a new platform to study the fundamental mechanism of SC and CDW in the kagome superconductors.

References

- 1 Jiang, Y.-X. *et al.* Unconventional chiral charge order in kagome superconductor KV_3Sb_5 . *Nat. Mater.* **20**, 1353, doi:10.1038/s41563-021-01034-y (2021).
- 2 Liang, Z. *et al.* Three-dimensional charge density wave and surface-dependent vortex-core states in a kagome superconductor CsV_3Sb_5 . *Phys. Rev. X* **11**, 031026, doi:10.1103/PhysRevX.11.031026 (2021).
- 3 Yu, F. H. *et al.* Unusual competition of superconductivity and charge-density-wave state in a compressed topological kagome metal. *Nat. Commun.* **12**, 3645, doi:10.1038/s41467-021-23928-w (2021).
- 4 Ortiz, B. R. *et al.* CsV_3Sb_5 : A Z_2 topological kagome metal with a superconducting ground state. *Phys. Rev. Lett.* **125**, 247002, doi:10.1103/PhysRevLett.125.247002 (2020).
- 5 Chen, K. Y. *et al.* Double superconducting dome and triple enhancement of T_c in the kagome superconductor CsV_3Sb_5 under high pressure. *Phys. Rev. Lett.* **126**, 247001, doi:10.1103/PhysRevLett.126.247001 (2021).
- 6 Yang, S.-Y. *et al.* Giant, unconventional anomalous Hall effect in the metallic frustrated magnet candidate, KV_3Sb_5 . *Sci. Adv.* **6**, eabb6003 (2020).
- 7 Yu, F. H. *et al.* Concurrence of anomalous Hall effect and charge density wave in a superconducting topological kagome metal. *Phys. Rev. B* **104**, L041103, doi:10.1103/PhysRevB.104.L041103 (2021).
- 8 Kenney, E. M., Ortiz, B. R., Wang, C., Wilson, S. D. & Graf, M. J. Absence of local moments in the kagome metal KV_3Sb_5 as determined by muon spin spectroscopy. *J. Phys. Condens. Matter* **33**, 235801, doi:10.1088/1361-648X/abe8f9 (2021).
- 9 Chen, H. *et al.* Roton pair density wave in a strong-coupling kagome superconductor. *Nature*, <https://doi.org/10.1038/s41586-41021-03983-41585> (2021).
- 10 Zhao, H. *et al.* Cascade of correlated electron states in a kagome superconductor CsV_3Sb_5 . *Nature* <https://doi.org/10.1038/s41586-41021-03946-w>, doi:<https://doi.org/10.1038/s41586-021-03946-w> (2021).
- 11 III, C. M. *et al.* Time-reversal symmetry-breaking charge order in a correlated kagome superconductor. *Arxiv:2106.13443* (2021).
- 12 Feng, X., Jiang, K., Wang, Z. & Hu, J. Chiral flux phase in the Kagome superconductor AV_3Sb_5 . *Sci. Bull.* **66**, 1384-1388, doi:10.1016/j.scib.2021.04.043 (2021).
- 13 Denner, M. M., Thomale, R. & Neupert, T. Analysis of charge order in the kagome metal AV_3Sb_5 *Arxiv:2103.14045* (2021).
- 14 Lin, Y.-P. & Nandkishore, R. M. Complex charge density waves at Van Hove singularity on hexagonal lattices: Haldane-model phase diagram and potential realization in kagome metals AV_3Sb_5 . *Arxiv:2104.02725* (2021).
- 15 Wu, X. *et al.* Nature of unconventional pairing in the kagome superconductors AV_3Sb_5 . *Arxiv:2104.05671* (2021).
- 16 Feng, X., Zhang, Y., Jiang, K. & Hu, J. Low-energy effective theory and symmetry classification of flux phases on Kagome lattice. *Arxiv:2106.04395* (2021).
- 17 Lin, Y.-P. Higher-order topological insulators from 3Q charge bond orders on hexagonal lattices: A hint to kagome metals. *Arxiv:2106.09717* (2021).
- 18 Miao, H. *et al.* Geometry of the charge density wave in kagome metal AV_3Sb_5 . *Arxiv:2106.10150* (2021).
- 19 Christensen, M. H., Birol, T., Andersen, B. M. & Fernandes, R. M. Theory of the charge-density wave in AV_3Sb_5 kagome metals. *Arxiv:2107.04546* (2021).

- 20 Tazai, R., Yamakawa, Y., Onari, S. & Kontani, H. Mechanism of exotic density-wave and beyond-Migdal unconventional superconductivity in kagome metal AV_3Sb_5 ($A=K, Rb, Cs$). *Arxiv:2107.05372* (2021).
- 21 Lin, Y.-P. & Nandkishore, R. M. Kagome superconductors from Pomeranchuk fluctuations in charge density wave metals. *Arxiv:2107.09050* (2021).
- 22 Gu, Y., Zhang, Y., Feng, X., Jiang, K. & Hu, J. Gapless excitations inside the fully gapped kagome superconductors AV_3Sb_5 . *Arxiv:2108.04703* (2021).
- 23 Park, T., Ye, M. & Balents, L. Electronic instabilities of kagome metals: Saddle points and Landau theory. *Phys. Rev. B* **104**, 035142, doi:10.1103/PhysRevB.104.035142 (2021).
- 24 Zhao, J., Wu, W., Wang, Y. & Yang, S. A. Electronic correlations in the normal state of the kagome superconductor KV_3Sb_5 . *Phys. Rev. B* **103**, L241117, doi:10.1103/PhysRevB.103.L241117 (2021).
- 25 Tan, H., Liu, Y., Wang, Z. & Yan, B. Charge density waves and electronic properties of superconducting kagome metals. *Phys. Rev. Lett.* **127**, 046401, doi:10.1103/PhysRevLett.127.046401 (2021).
- 26 Ortiz, B. R. *et al.* Superconductivity in the Z_2 kagome metal KV_3Sb_5 . *Phys. Rev. Mater.* **5**, 034801, doi:10.1103/PhysRevMaterials.5.034801 (2021).
- 27 Zhao, C. C. *et al.* Nodal superconductivity and superconducting dome in the topological Kagome metal CsV_3Sb_5 . *Arxiv:2102.08356* (2021).
- 28 Duan, W. *et al.* Nodeless superconductivity in the kagome metal CsV_3Sb_5 . *Arxiv:2013.11796* (2021).
- 29 Chao Mu, Q. Y., Zhijun Tu, Chunsheng Gong, Hechang Lei, Zheng Li, & Luo, J. S-Wave Superconductivity in Kagome Metal CsV_3Sb_5 Revealed by $^{121/123}Sb$ NQR and ^{51}V NMR Measurements. *Chin. Phys. Lett.* **38**, 077402, doi:10.1088/0256-307x/38/7/077402 (2021).
- 30 Paglione, J. & Greene, R. L. High-temperature superconductivity in iron-based materials. *Nat. Phys.* **6**, 645-658, doi:10.1038/nphys1759 (2010).
- 31 Fischer, Ø., Kugler, M., Maggio-Aprile, I., Berthod, C. & Renner, C. Scanning tunneling spectroscopy of high-temperature superconductors. *Rev. Mod. Phys.* **79**, 353-419, doi:10.1103/RevModPhys.79.353 (2007).
- 32 Scalapino, D. J. A common thread: The pairing interaction for unconventional superconductors. *Rev. Mod. Phys.* **84**, 1383-1417, doi:10.1103/RevModPhys.84.1383 (2012).
- 33 Stewart, G. R. Superconductivity in iron compounds. *Rev. Mod. Phys.* **83**, 1589-1652, doi:10.1103/RevModPhys.83.1589 (2011).
- 34 Song, Y. *et al.* Competition of superconductivity and charge density wave in selective oxidized CsV_3Sb_5 thin flakes. *Arxiv:2105.09898* (2021).
- 35 Wang, Q. *et al.* Charge Density Wave Orders and Enhanced Superconductivity under Pressure in the Kagome Metal CsV_3Sb_5 . *Adv. Mater.*, 2102813, doi:10.1002/adma.202102813 (2021).
- 36 Tsirlin, A. A. *et al.* Role of Sb in the superconducting kagome metal CsV_3Sb_5 revealed by its anisotropic compression. *Arxiv:2007.15228* (2021).
- 37 Zhu, C. C. *et al.* Double-dome superconductivity under pressure in the V-based Kagome metals AV_3Sb_5 ($A = Rb$ and K). *Arxiv:2104.14487* (2021).
- 38 Du, F. *et al.* Evolution of superconductivity and charge order in pressurized RbV_3Sb_5 . *Arxiv:2108.09434* (2021).
- 39 Zhang, Z. *et al.* Pressure-induced reemergence of superconductivity in the topological kagome metal CsV_3Sb_5 . *Phys. Rev. B* **103**, 224513, doi:10.1103/PhysRevB.103.224513 (2021).

- 40 Du, F. *et al.* Pressure-induced double superconducting domes and charge instability in the
kagome metal KV_3Sb_5 . *Phys. Rev. B* **103**, L220504, doi:10.1103/PhysRevB.103.L220504
(2021).
- 41 Pennycook, S. J. & Boatner, L. A. Chemically sensitive structure-imaging with a scanning-
transmission electron-microscope. *Nature* **336**, 565-567, doi:DOI 10.1038/336565a0 (1988).
- 42 Xu, H.-S. *et al.* Multiband superconductivity with sign-preserving order parameter in kagome
superconductor CsV_3Sb_5 . *Arxiv:2104.08810* (2021).
- 43 Li, H. *et al.* No indication of chiral flux current in the topological kagome metal CsV_3Sb_5 .
Arxiv:2107.11326 (2021).
- 44 Wang, Z. *et al.* Electronic nature of chiral charge order in the kagome superconductor CsV_3Sb_5 .
Phys. Rev. B **104**, doi:10.1103/PhysRevB.104.075148 (2021).
- 45 Xiang, Y. *et al.* Nematic electronic state and twofold symmetry of superconductivity in the
topological kagome metal CsV_3Sb_5 . *Arxiv:2104.06909* (2021).
- 46 Ni, S. *et al.* Anisotropic Superconducting Properties of Kagome Metal CsV_3Sb_5 . *Chin. Phys.*
Lett. **38**, 057403, doi:10.1088/0256-307x/38/5/057403 (2021).
- 47 Dong, X. *et al.* $(\text{Li}_{0.84}\text{Fe}_{0.16})\text{OHFe}_{0.98}\text{Se}$ superconductor: Ion-exchange synthesis of large single-
crystal and highly two-dimensional electron properties. *Phys. Rev. B* **92**, 064515 (2015).
- 48 Safar, H. *et al.* Experimental evidence for a first-order vortex-lattice-melting transition in
untwinned, single crystal $\text{YBa}_2\text{Cu}_3\text{O}_7$. *Phys. Rev. Lett.* **69**, 824-827,
doi:10.1103/PhysRevLett.69.824 (1992).
- 49 Blatter, G., Feigel'man, M. V., Geshkenbein, V. B., Larkin, A. I. & Vinokur, V. M. Vortices in
high-temperature superconductors. *Rev. Mod. Phys.* **66**, 1125 (1994).
- 50 Eltsev, Y. *et al.* Anisotropic superconducting properties of MgB_2 single crystals probed by in-
plane electrical transport measurements. *Phys. Rev. B* **65**, 140501 (2002).

Main Figures

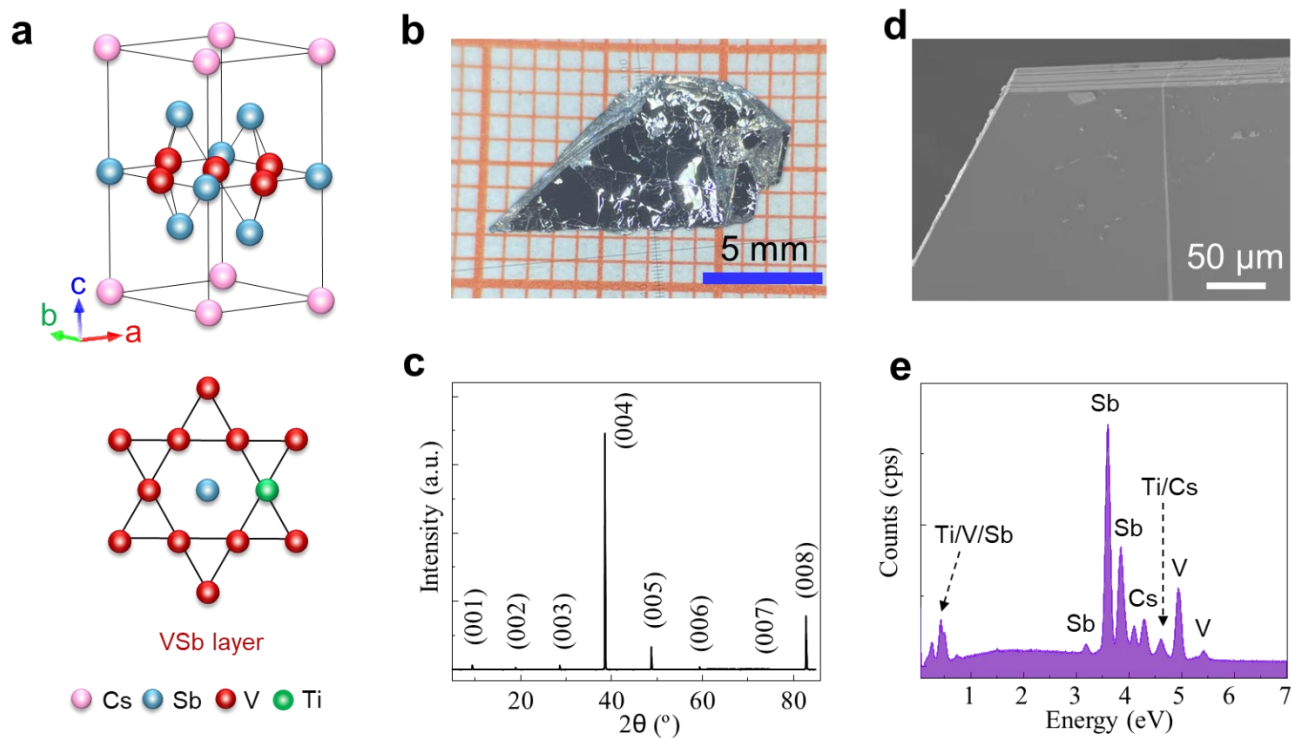


Fig. 1. Crystalline structure, structure characterization, and stoichiometric ratio of the Ti-doped $\text{CsV}_{3-x}\text{Ti}_x\text{Sb}_5$. **a**, Schematic of atomic structure of Ti-doped $\text{CsV}_{3-x}\text{Ti}_x\text{Sb}_5$ crystal with Cs atoms in light purple, Sb atoms in light blue, V atoms in red and Ti atoms in green. The Ti atoms replace the V atoms in Kagome lattice. **b**, A photo of a single crystal of the as-prepared Ti-doped $\text{CsV}_{3-x}\text{Ti}_x\text{Sb}_5$ ($x=0.15$) crystal. **c**, Typical XRD pattern of the Ti-doped $\text{CsV}_{3-x}\text{Ti}_x\text{Sb}_5$ ($x=0.15$) crystal. **d**, The SEM image of the Ti-doped $\text{CsV}_{3-x}\text{Ti}_x\text{Sb}_5$ ($x=0.15$) crystal showing the uniform structure at the surface. **e**, EDS of the crystal showing the stoichiometric ratio of Cs:V:Ti:Sb = 0.96:2.85:0.15:4.95.

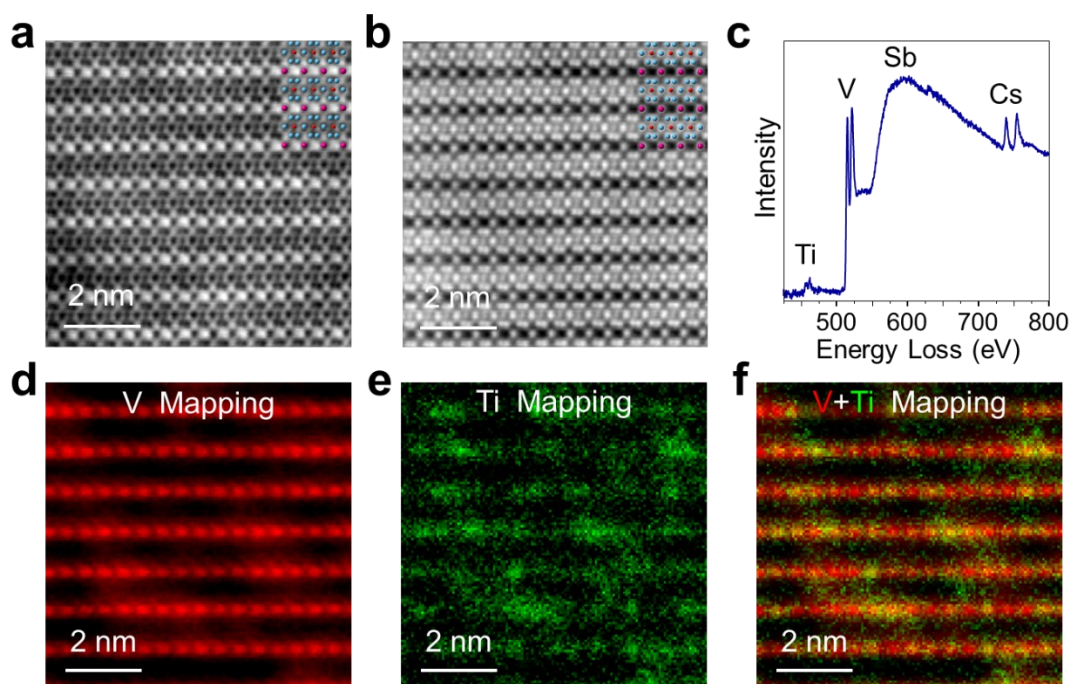


Fig. 2. Atomic-scale structural and chemical analysis of Ti-doped $\text{CsV}_{3-x}\text{Ti}_x\text{Sb}_5$. **a, b** Simultaneously acquired atomic resolution STEM-ABF image (**a**) and STEM-HAADF Z-contrast image (**b**) of Ti-doped $\text{CsV}_{3-x}\text{Ti}_x\text{Sb}_5$ crystal viewed along the $[100]$ projection, with the atomic structural models overlaid. The Cs, V, Sb atoms are shown in purple, red, and light blue, respectively. **c**, Background-subtracted EELS spectrum showing clear Ti, V, Sb, and Cs signals. Quantification of the Ti and V signals shows an atomic ratio of $\text{Ti}:\text{V} \sim 5.3:94.7$. Note that this analysis is only semi-quantitative due to errors in calculating the inelastic scattering cross-sections for the different element edges. **d,e**, Atomic-resolution chemical mapping acquired via STEM-EELS spectrum imaging, with the simultaneously acquired V mapping shown in red (**d**) and Ti mapping shown in green (**e**). **f**, Overlay of the V (red) and Ti (green) signals. Ti is mostly doped into the V sites.

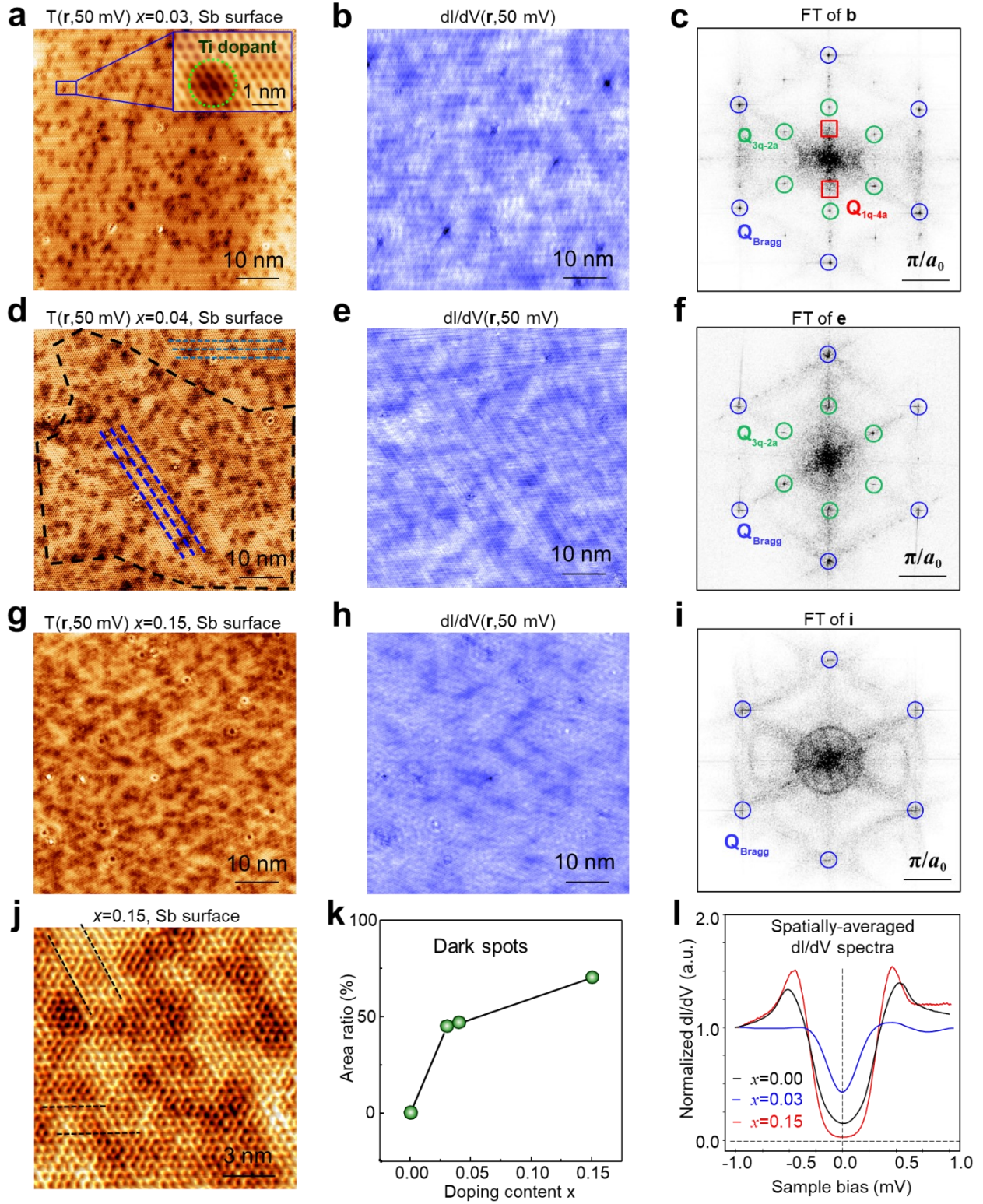


Fig. 3. STM images, dI/dV spectra and dI/dV mapping for the comparison of CDW states and superconducting gap of Ti-doped $\text{CsV}_{3-x}\text{Ti}_x\text{Sb}_5$ between $x=0.03$ and $x=0.15$. **a-c**, STM topography (**a**),

$dI/dV(r, -5\text{mV})$ (**b**) and the corresponding drift-corrected Fourier transform (FT) (**c**) at the large-scale Sb surface of $\text{CsV}_{3-x}\text{Ti}_x\text{Sb}_5$ ($x=0.03$) obtained at 4 K, showing the $3Q-2a$ and $1Q-4a$ CDWs. Many dark spots appear correlated to the Ti dopants in the STM image of (a). The Insert in (a): Zoom-in STM image showing the continuous lattice around the dark spots. **d-f**, STM topography (**d**), $dI/dV(r, -5\text{mV})$ (**e**) and the corresponding drift-corrected FT (**f**) at the large-scale Sb surface of $\text{CsV}_{3-x}\text{Ti}_x\text{Sb}_5$ ($x=0.04$), showing the presence of short-ranged $1Q-4a$ CDW multiple domains. Two $4a$ CDW domains can be clearly observed (highlighted by the blue and light blue dotted lines). **h-j**, STM topography (**h**), $dI/dV(r, -5\text{mV})$ (**i**) and the corresponding drift-corrected FT (**j**) at the large-sized Sb surface of $\text{CsV}_{3-x}\text{Ti}_x\text{Sb}_5$ ($x=0.15$), showing the absence of $3Q-2a$, $1Q-4a$ CDW states in the FT. **k**, Typical small-scale STM image of the $\text{CsV}_{3-x}\text{Ti}_x\text{Sb}_5$ ($x=0.15$) sample. Small patches of local $4a_0$ modulations can be observed (guided by the white dotted lines). **l**, Relationship between the doping content and the area ratio of the dark spots in the STM images, indicating that the dark spots in the STM images origin from Ti dopant in the underlying VSb layer. **m**, Spatially-averaged dI/dV spectra obtained on the Sb surface of the undoped (black curve), $\text{CsV}_{3-x}\text{Ti}_x\text{Sb}_5$ ($x=0.03$) (blue curve) and $\text{CsV}_{3-x}\text{Ti}_x\text{Sb}_5$ ($x=0.15$) samples, showing a transition from V-shape to U-shape symmetry through Ti doping. Setting parameter: tunneling current setpoint $I_s=1.0$ nA. Bias modulations in (l): $V_{mod}=0.05$ mV.

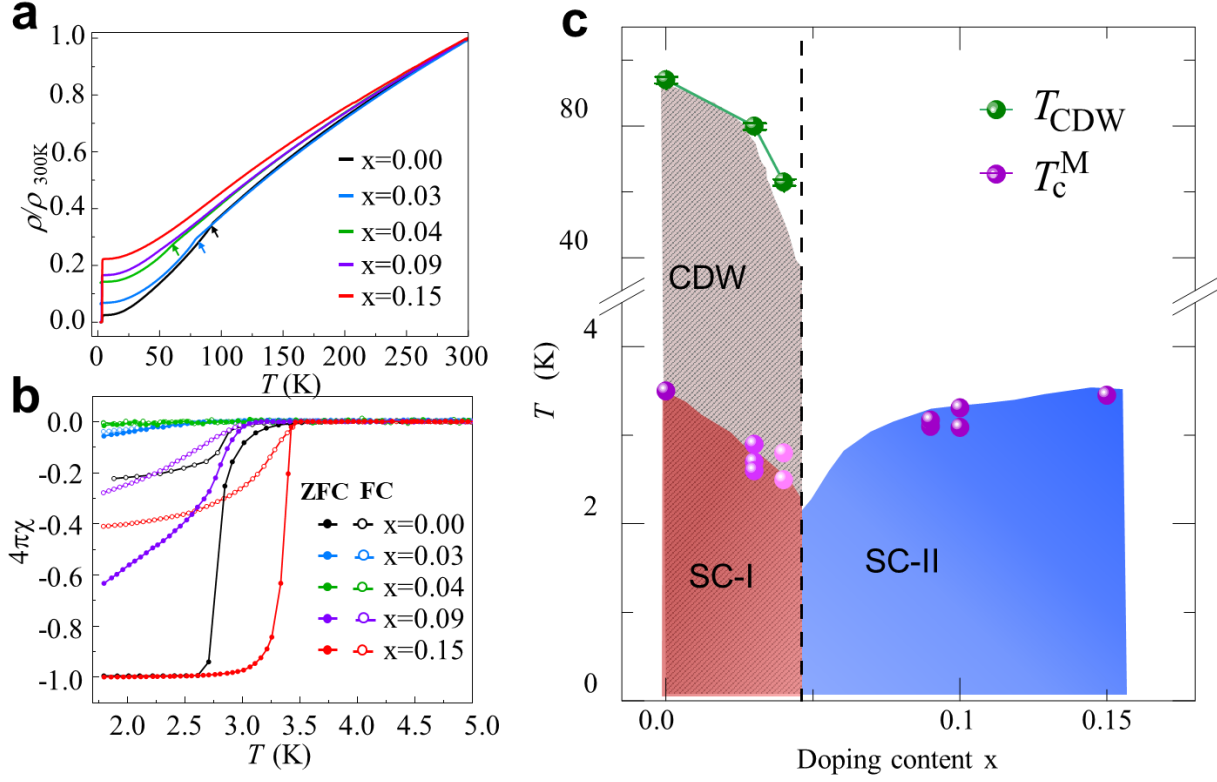


Fig. 4. Electrical transport, magnetic properties and phase diagram of $\text{CsV}_{3-x}\text{Ti}_x\text{Sb}_5$ crystals. **a**, The electrical resistivity of $\text{CsV}_{3-x}\text{Ti}_x\text{Sb}_5$ crystals with x from 0 to 0.15. The CDW is suppressed upon increasing x and undetectable when x exceeds 0.09. **b**, The temperature-dependent magnetic susceptibilities corrected for demagnetization factor under zero-field cooling (ZFC) and field cooling (FC, 1 Oe along the c axis). Bulk superconductivity is confirmed by the diamagnetism. **c**, Phase diagram of the $\text{CsV}_{3-x}\text{Ti}_x\text{Sb}_5$ crystals. In the SC-I regime, T_{CDW} and T_c^M are significantly reduced with increasing x . In the SC-II regime, the superconductivity tends to gradually increase: T_c^M rises from ~ 3 K at $x = 0.09$ to ~ 3.5 K at $x = 0.15$.

Acknowledgements

We thank Zhong-Xian Zhao and Gang Su for helpful discussions. The work is supported by grants from the National Natural Science Foundation of China (61888102, 52022105, 51771224, 12061131005 and 11834016), the National Key Research and Development Projects of China (2017YFA0206303, 2018YFA0305800 and 2019YFA0308500), the Chinese Academy of Sciences (XDB33030100, XDB28000000, and XDB30000000), and the Beijing Outstanding Young Scientist Program (BJJWZYJH01201914430039). Z.W. is supported by the US DOE, Basic Energy Sciences Grant No. DE-FG02-99ER45747.

Author Contributions: H.-J.G. designed the experiments and supervised the project. H.Y. and Z.Z. prepared the samples. Y.Z., Z.L., H.Z., H.Y. and X.D. performed the transport experiments. H.C., Z.H., G.Q., and B.H. performed the STM experiments with guidance of H.-J.G. W.Z., J.S. and S.J.P. performed the STEM experiments. All authors participated in the data analysis and manuscript writing.

Competing Interests: The authors declare that they have no competing interests.

Data availability

Data measured or analyzed during this study are available from the corresponding author on reasonable request.